Article

Damage on a Solid–Liquid Interface Induced by the Dynamical Behavior of Injected Gas Bubbles in Flowing Mercury

Hiroyuki Kogawa *, Takashi Wakui and Masatoshi Futakawa

Japan Atomic Energy Agency, Ibaraki 319-1195, Japan
* Correspondence: kogawa.hiroyuki@jaea.go.jp

Abstract: Microbubbles have been applied in various fields. In the mercury targets of spallation neutron sources, where cavitation damage is a crucial issue for life estimation, microbubbles are injected into the mercury to absorb the thermal expansion of the mercury caused by the pulsed proton beam injection and reduce the macroscopic pressure waves, which results in reducing the damage. Recently, when the proton beam power was increased and the number of injected gas bubbles was increased, unique damage morphologies were observed on the solid–liquid interface. Detailed observation and numerical analyses revealed that the microscopic pressure emitted from the gas bubbles contracting is sufficient to form pit damage, i.e., the directions of streak-like defects which are formed by connecting the pit damage coincides with the direction of the gas bubble trajectories, and the distances between the pits was understandable when taking the natural period of gas bubble vibration into account. This indicates that gas microbubbles, used to reduce macroscopic pressure waves, have the potential to be inceptions of cavitation damage due to the microscopic pressure emitted from these gas bubbles. To completely mitigate the damage, we have to consider the two effects of injecting gas bubbles: reducing macroscopic pressure waves and reducing the microscopic pressure due to bubble dynamics.

Keywords: microbubble; mercury target; cavitation damage; pressure wave; solid–liquid interface; impact pressure; gas bubble vibration

1. Introduction

Microbubbles have been applied in various fields. For example, they are used to reduce flow resistance by controlling the boundary layer in ships [1], to clean semiconductors by using microscopic impact pressure emitted during bubble collapse [2], and more, including as contrast agents in ultrasounds in the medical field [3]. In mercury targets, which are high-intensity spallation neutron sources, microbubbles are injected into the mercury to absorb the rapid thermal expansion of mercury. The neutron beams produced in the mercury target are applicable to create innovative research. Neutron beams are produced by spallation reactions when pulsed proton beams are injected into heavy metals. In high-power spallation neutron source facilities such as the SNS in the US [4] and the MLF/J-PARC [5], liquid mercury is used as the target material from the viewpoint of both neutron yield efficiency and cooling performance. Pulsed proton beam injections (pulse duration, 1 μs; repetition cycle, 25 Hz) cause macroscopic pressure waves (hereafter, called MACP) due to the rapid thermal expansion of mercury. Cavitation incidents [6,7] induce the nearby interface between the structure wall and the liquid mercury in the process of MACP propagation in the mercury target vessel. As such, cavitation damage is imposed on the vessel wall [8,9]. This cavitation damage becomes one of crucial issues for keeping

the structural integrity and prolonging the lifetime of the target vessels. In order to reduce the MACPs, the gas bubbles were injected into the flowing mercury to absorb the rapid thermal expansion through the mechanism of the bubbles' contraction, and thereby the cavitation damage is expected to be mitigated [10–12]. On the other hand, microscopic pressure (hereafter, called MICP) is emitted by the vibration of injected gas bubbles which is excited by MACPs. The MICPs emitted by gas bubble vibrations are deduced to have two kinds of effects: one is positive, and another is negative. As for the positive effect, the inception of cavitation bubbles may be suppressed by the MICPs, a so called "suppression effect" [13,14]. As for the negative effect, these gas bubbles could become cavitation nuclei, which should be considered carefully.

It was confirmed by measuring the vibration of the vessel wall using a laser Doppler vibration (LDV) system during the operation of mercury targets in MLF that the MACPs were dramatically reduced by injecting gas bubbles, which resulted in decreases in the cavitation damage. Nevertheless, damage, inferred to be caused by the MICPs emitted by the gas bubbles vibrations, was observed. The pits, which are generated by cavitation damage, were much shallower in depth and wider in radius under the gas bubble injection conditions compared to the pits generated without gas bubble injection. And, damage morphology was observed with these features as follows.

(1) Streak-like defects were observed, and the directions roughly coincided with the flow direction of the injected gas bubbles, which was evaluated through computational fluid dynamics (CFD) on the flowing bubble distribution.
(2) Series of beaded pits were observed in the streak-like defects. The distances between each pit were wider in the upper area than in the lower area, which indicated a correlation that bubble size distribution was affected by the buoyancy.

In this paper, the damage morphology observed in the mercury target vessel is described in detail, and the damage generation mechanism by the gas bubbles is discussed qualitatively. The MICP emitted by a single gas bubble vibration, P_L, was estimated based on the bubble dynamics. And, the MICP applied on the solid wall, P_{imp}, was estimated, considering the distance between the gas bubbles and the solid wall; the damage mechanism due to the MICPs emitted by the gas bubbles is discussed.

2. Damage Morphology Observation

2.1. The Effect of Gas Bubbles on the (Macroscopic Pressure Wave)–Materials and Methods

Figure 1 shows the cross-sectional view of the mercury target vessel in J-PARC. The mercury was enclosed with a mercury target vessel. The material of the mercury target vessel was type 316 L stainless steel. The proton beams were injected through its tip (called the beam window). The mercury flowed from the inlet side to the other side of the target vessel. Flow guide vanes were installed in the target vessel so that the mercury flowed across the proton beam injection path at the horizontal center of the vessel. A bubble generator was installed at the mercury inlet side [11]. Since the heat generation in the mercury owing to the proton beam injection was highest near the center of the beam window, and the amplitude of the generated pressure wave (MACP) was also larger there, the specimen for observing the damage was cut out from the center of the beam window after the operation [15]. The bubble generator was about 400 mm away from the beam window. Near the beam window, more bubbles were distributed on the upper area rather than on the lower area in the direction of gravity due to buoyancy. Figure 2 shows the distribution of the gas bubble radius obtained by computational fluid dynamics (CFD) in the upper and lower areas in the mercury near the cut-out specimen [16]. Many of the gas bubbles with larger sizes were distributed in the upper area compared to the lower area.
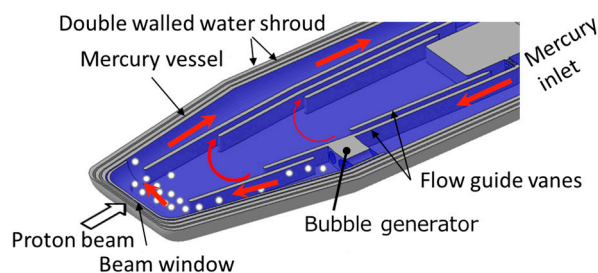
Figure 1. Cross sectional view of a mercury target vessel. Pulsed proton beams were injected at a beam window. The mercury flowed from one side to another side. At the horizontal center, mercury flowed in, perpendicular to the proton beam's injected direction. The bubble generator was set on the inlet side.
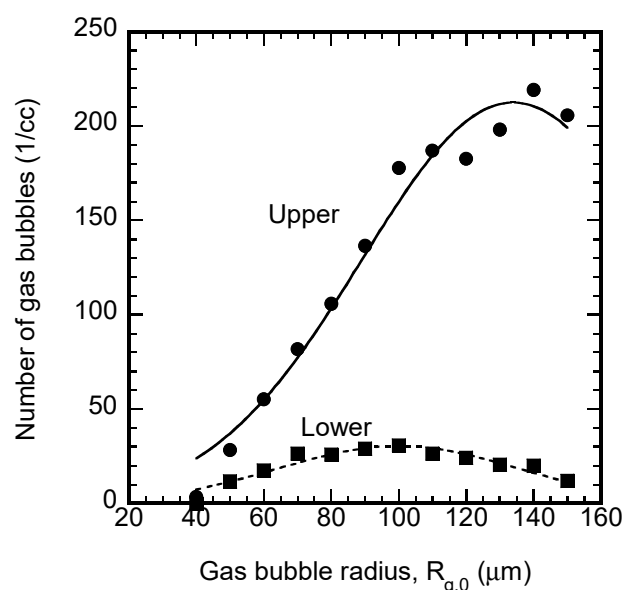
Figure 2. The gas bubble population near the beam window calculated by CFD. Many gas bubbles were distributed in the upper area because of buoyancy. The mean bubble radius was larger in the upper area than that in the lower area.

Figure 3a,b show photographs of the damage observed on the specimens cut out after operations in the cases that the amount of gas supply used to bubble was low and relatively high, respectively. In the case of Figure 3a, gas was not supplied for 30% of the entire operation period because of trouble within the gas supplying system. The proton beam conditions in Figure 3a,b were 530 kW and 570 kW in the average power, and 165 days and 121 days in the operation time, respectively. That is, the accumulated beam powers were almost the same between the cases shown in Figure 3a,b. In Figure 3a, the maximum depth of damage reached 3.3 mm for a wall thickness of 5 mm. On the other hand, in Figure 3b, the maximum depth decreased to 0.4 mm, confirming a damage mitigation effect owing to the reduction in the MACPs due to gas bubble injection. The maximum depth occurred at the center of the gravity direction where the MACP was highest in Figure 3a, while in Figure 3b, it was observed in the lower area. This is thought to be due not only to the reduction in MACPs but also to the suppression effect of gas bubbles [13,14], which suppresses the inception of cavitation in the upper region where more bubbles are distributed, as shown in Figure 2. These results suggest that this number of gas bubbles is effective for the damage mitigation. Furthermore, the fatigue damage combined with cavitation erosion was recognized strongly in the case of Figure 3a. The fatigue phenomenon was also mitigated, owing to the reduction in MACPs by the higher number of gas bubbles as shown in Figure 3b. The fatigue damage was complicated and

included uncertainty factors including material degradation due to irradiation and/or LME (liquid metal embrittlement), etc. That is, it is essential from the viewpoint of lifetime estimation to eliminate the fatigue phenomenon caused by the MACPs as well.


(a)　　　　　　　　　　　　　　　　(b)
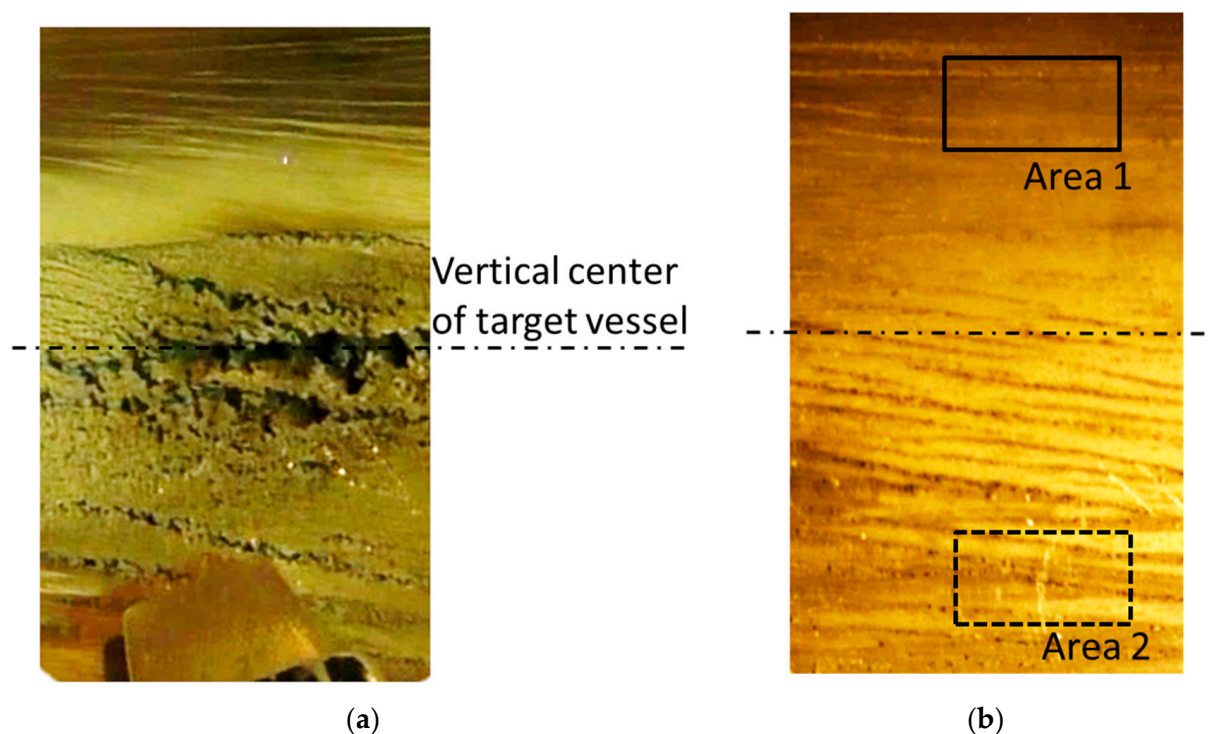
Figure 3. Damage at the beam window in contact with mercury in the cases of (**a**) low gas bubble injection and (**b**) relatively high gas bubble injection. Damage was mitigated in (**b**) but inclined streak-like defects were observed.

2.2. The Effect of MICP (Microscopic Pressure) Emitted from Gas Bubbles

Detailed observation of Figure 3b revealed many streak-like defects tilted downward relative to the horizontal direction, i.e., the primary flow direction of mercury. Since the gas bubbles were injected into the flowing mercury by using a swirling flow into the mercury target [11], the trajectories of the injected gas bubbles may have also been tilted to the horizontal direction. Figure 4 shows the trajectories of the injected gas bubbles on the interface between the mercury and the wall of the mercury target vessel calculated by CFD. It was noted that the darker colors indicated the trajectory of larger size bubbles. Although a mixture of trajectories of large and small gas bubbles was recognized near the vertical center, it was recognized that many large bubbles flowing in the upper section and many small bubbles flowing in the lower section. The trajectories were tilted downward to the direction of the primary flow of mercury. Compared to Figure 3b, the tilted slope of the observed streak-like damage was consistent with the trajectories of the injected gas bubbles. This result suggested that the injected gas bubbles are affecting the damage.

Furthermore, beaded pits were observed in the streak-like defects as shown in Figure 5a,b, which show detailed observations in the streak-like defects in the upper (Area 1 in Figure 3b) and lower (Area 2 in Figure 3b) areas, respectively. The distance to the next pit, ΔD, was relatively wide in the upper area shown in Figure 5a than that in the lower area shown in Figure 5b. These observation results seemed to correlate with the radius of the distributed gas bubbles.
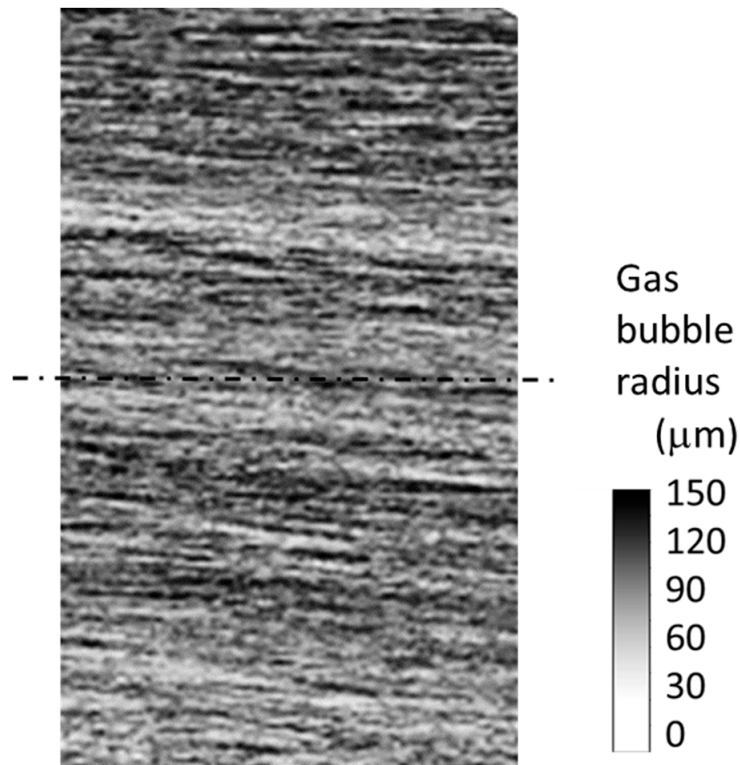
Figure 4. Gas bubble trajectories obtained by CFD analysis. Swirl flow, generated in a bubble generator, affected the slopes of the trajectories, which were similar with those of the streak-like defects observed in Figure 3b.
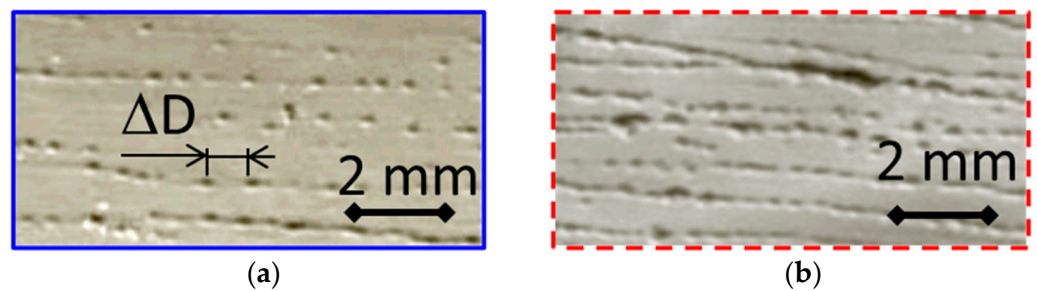
Figure 5. Detailed observation of the streak-like defects in (**a**) Area 1 and (**b**) Area 2 in Figure 3b. Beaded pits were observed in the streak-like defects. The distance to the next pit, ΔD, was relatively narrow in the lower area in (**b**).

Therefore, we considered the possibility that the gas bubbles, injected to absorb thermal expansion and reduce MACPs, could become the inception of damage. We focused on the natural period, T_0, of the gas bubbles and estimated the distance to the next pit, ΔD_{CFD}, with the following assumptions based on the distribution of the gas bubbles shown in Figure 2.

Pits are formed by repeated MICPs due to the repeated expansion and collapse (vibration) of gas bubbles flowing in mercury.

The natural period, T_0, of a bubble estimated by Equation (1) [17] depends on the bubble radius, $R_{g,0}$ (where the larger the bubble, the longer the T_0).

$$T_0(R_{g,0}) = R_{g,0}\Big/\sqrt{\frac{3\gamma}{\rho_L}\left(p_\infty + \frac{2\sigma}{R_{g,0}}\right) - \frac{2\sigma}{\rho_L R_{g,0}}} \qquad (1)$$

where $R_{g,0}$ is the initial radius of the gas bubble, γ is the specific heat ratio of gas, ρ_L is the density of liquid, and p_∞ is the liquid pressure at a distance.

The bubble flows in mercury, and the flow speed of the bubble is represented by v_{Hg}. Thus, ΔD_{CFD} at any initial bubble radius can be calculated as

$$\Delta D_{CFD} = v_{Hg} \times T_0\left(R_{g,0}\right) \tag{2}$$

Figure 6a,b show the comparisons of the distributions between ΔD_{CFD} and the observed ΔD for the upper area (Figure 5a) and the lower area (Figure 5b), respectively. The observed distribution of ΔD was similar to the distribution of ΔD_{CFD} based on the estimation. The peak value of ΔD was wider in Area 1 (upper part) where many large bubbles were distributed. The results of these studies indicated that the distribution of the gas bubble radius correlated with the distribution of ΔD, and that the gas bubbles injected to reduce thermal expansion may become cavitation nuclei and cause damage.
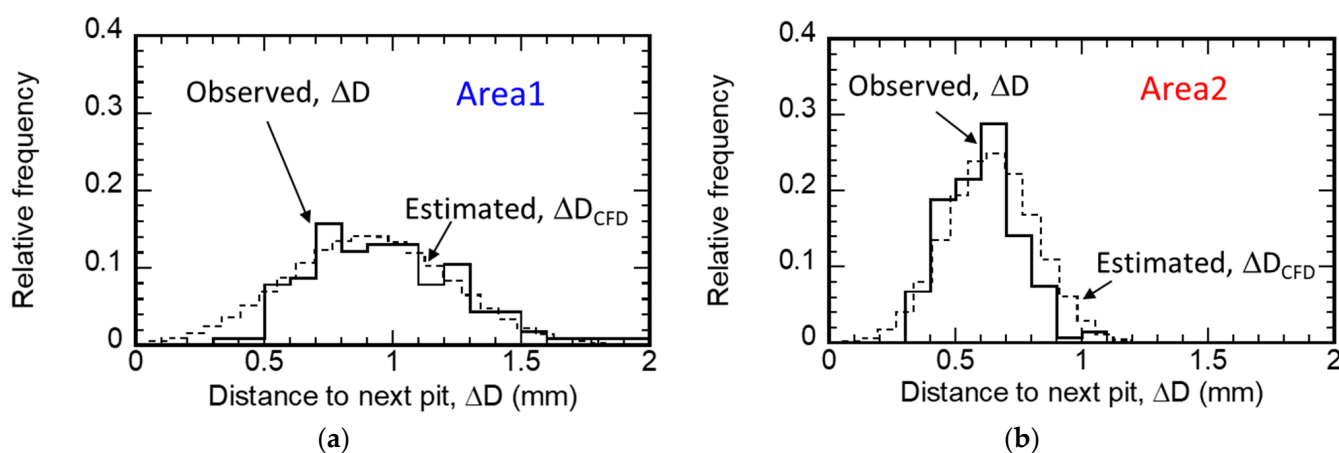
Figure 6. Comparison of the ΔD_{CFD} distribution based on the bubble distribution by CFD and the observed ΔD distribution for the (**a**) upper area (Figure 5a) and (**b**) lower area (Figure 5b). The observed distribution of ΔD was similar to the distribution of ΔD_{CFD}. The correlation between bubble size and damage was recognized.

In the damage observation, not only were beaded pits observed in the streak-like defects, but also isolated pits that were not on the streak-like defects. Morphologies of the isolated pits, which are considered to be the initiation for the formation of streak-like defects, were measured. The pit morphologies for depth, D_{max}, and equivalent radius, R_d, were measured with a One-shot 3D Measurement Macroscope VR-3200 (KEYENCE, Osaka, Japan). The equivalent radius, R_d, was calculated, assuming that the area of the measured pit was a circle. Figure 7 shows the relationship between the maximum pit depth, D_{max}, and the pit radius, R_d, of the isolated pits observed in Area 1 and Area 2 of Figure 3b. D_{max} in Area 1 and Area 2 were distributed with similar variations, but the R_d tended to be larger in Area 1, where larger gas bubbles existed. This suggested that the size of the gas bubbles affects the size of the damage. Furthermore, the isolated pits observed in this study tended to have a larger radius and shallower depth than the ones formed by microjets during cavitation collapse when microbubbles were not injected [7,18]. These results also suggested that the isolated pits observed in this study were formed by a different mechanism than the pits caused by microjets.
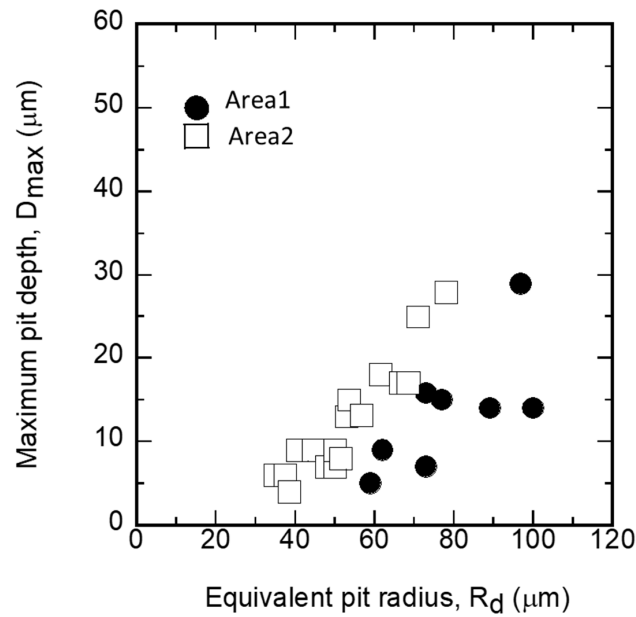
Figure 7. Relationship between the maximum pit depth, D_{max}, and the pit radius, R_d, of the isolated pits observed in Area 1 and Area 2 of Figure 3b. The D_{max} in Area 1 and Area 2 were distributed with similar variations, but the R_d tended to be larger in Area 1, where larger gas bubbles existed.

3. Numerical Analysis

The observed damage results and analyses on the damage indicated that the gas bubbles, injected to reduce MACPs, had the potential to be nuclei of cavitation. As for the isolated pits, those were shallow and wide in Area 1 compared to those in Area 2. The gas bubble sizes near Area 1 and Area 2 were different. In order to investigate the effect of gas bubble size on the formation of pits, the MICP applied on the solid wall was estimated by numerical analysis, and the formation mechanism of the observed pits were considered. At first, the MICP emitted by vibration of a single gas bubble was estimated based on bubble dynamics. Next, the MICP applied on the solid wall was estimated considering the distance between the gas bubble and the solid wall.

3.1. The Estimation of MICP Emitted by Gas Bubble Vibration

First, the Keller-Miksis equation in Equation (3) [19] was used to calculate the pressure at the bubble surface, which was the MICP emitted by gas bubble vibrations.

$$\left(1 - \frac{1}{c_L}\dot{R}_g\right) R_g\ddot{R}_g + \frac{3}{2}\left(1 - \frac{1}{3c_L}\dot{R}_g\right)\dot{R}_g^2 = \frac{1}{\rho_L}\left(1 + \frac{1}{c_L}\dot{R}_g\right)\left(p_L - p_\infty\left(t + \frac{R_g}{c_L}\right)\right) + \frac{\dot{p}_L}{\rho_L c_L}R_g \tag{3}$$

where c_L is the sound velocity, p_g is the pressure inside the bubble was estimated by Equation (4), and the pressure at the bubble interface, p_L, was estimated by Equation (5).

$$p_g(R) = \left(p_{\infty 0} - p_v + \frac{2\sigma}{R_{g,0}}\right)\left(\frac{R_{g,0}}{R_g}\right)^{3\gamma} \tag{4}$$

$$p_L = p_g - \frac{1}{R}\left(2\sigma + 4\mu\dot{R}_g\right) + p_v \tag{5}$$

The change in MACP around the bubble, p_∞, was given as in Figure 8, simplifying the change in the mercury target, since the duration of the negative pressure in the mercury near the target vessel lasted for a few milliseconds in the pressure wave analysis of the mercury target [12]. The estimation was performed by systematically varying $R_{g,0}$, $p_{\infty,0}$, and t_1 at 40~500 μm, −0.040~0 MPa, and 1~5 ms, respectively.
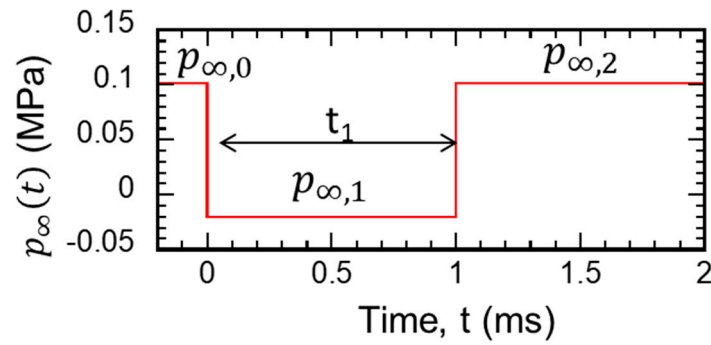
Figure 8. The pressure change around a gas bubble. This time history was used for bubble dynamics calculations in Equation (3).

Figure 9 shows the time behaviors of the gas bubble radius and the pressure at the bubble interface under the condition that the initial gas bubble radius, $R_{g,0}$, was 100 μm, and that the pressure around the gas bubble, $p_{\infty,0}$, decreased stepwise from atmospheric pressure to $p_{\infty,1} = -0.02$ MPa for $t_1 = 1$ ms then returned to atmospheric pressure. While the pressure, p_∞, was negative, the bubble continued to expand. When the pressure changed to positive, the bubble began to contract and reached a minimum radius. The gas bubble then oscillated through repeated expansion and contraction. As the bubble contracted, the pressure at the bubble interface increased. The increasing pressure at the bubble interface was greatest at the initial contraction, and then local impact pressure at the bubble interface decreased with the number of repetitions. Under the conditions shown in Figure 9, the local impact pressures at the bubble interface exceeded the 0.2% proof stress of the mercury target vessel material up to the fifth repetition. As shown in Equation (3), the density and surface tension of the liquid affect the bubble behavior and the pressure at the bubble interface. The density and surface tension of mercury were about 13.5 and 6.7 times higher than those of water, respectively. These effects on the local impact pressure at the bubble interface, p_L, was estimated. As a result, the pressure, p_L in mercury was 10 times higher than that in water when $R_{g,0}$ = 100 μm, $p_{\infty,1} = -0.02$ MPa, and $t_1 = 5$ ms.
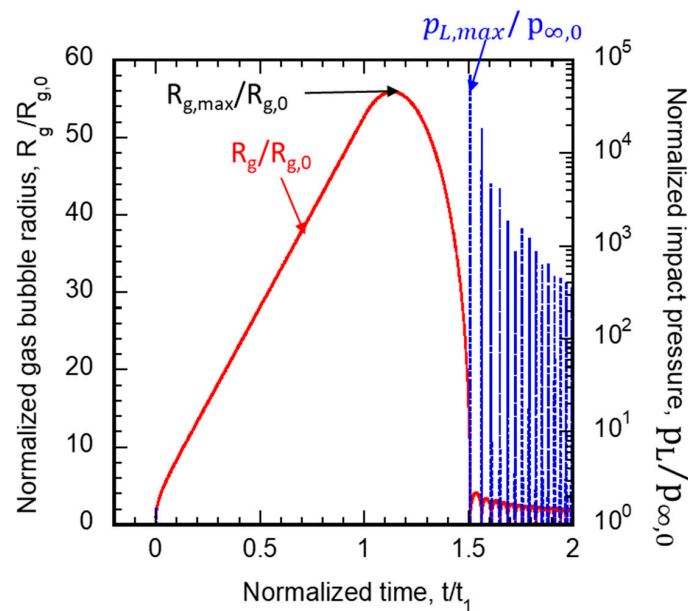

Figure 9. Time behaviors of the gas bubble radius and the pressure at the bubble interface at $R_{g,0} = 100$ μm, $p_{\infty,1} = -0.02$ MPa for $t_1 = 5$ ms. An impact pressure exceeding the 0.2% proof stress of the wall material was generated, which indicated that the local impact pressure generated from the gas bubble had the potential to form a pit on the wall surface.

3.2. The Estimation of MICP Applied on a Solid Wall

Figure 10 shows a schematic diagram of the analysis for the estimation of MICP applied on a solid wall. Here, for the simple estimation of whether the MICP applied to the solid wall from the gas bubble vibration was enough to generate the damage, the following were assumed:

(a) There is no collapse of the bubbles, which would be accompanied by microjets since the correlation between the observed distance to the next pit, ΔD, and the natural period of the existing gas bubbles was recognized, as shown in Figure 6;

(b) The maximum pressure generated at the bubble interface when a single bubble contracted at an arbitrary distance from the solid wall, h, propagated as a spherical wave [20].
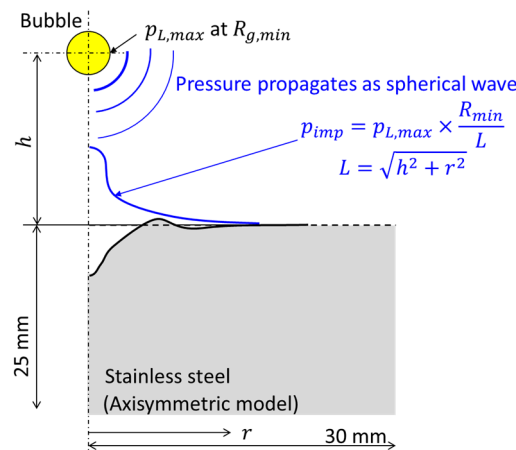
Figure 10. Schematic diagram of the analysis for the calculation of pit morphology. For analysis, the applied pressure on the wall surface was assumed that the local impact pressure, $p_{L,max}$, generated on the bubble surface propagated as a spherical wave. The applied pressure on the solid wall was expressed by $p_{imp}(r)$.

Therefore, the MICP applied on the solid wall, $P_{imp}(r)$, was estimated by using the general equation for the distance decay of pressure for a spherical wave in liquid, as shown in Equation (6).

$$P_{imp}(r) = p_{L,max} \times \frac{R_{g,min}}{L} \tag{6}$$

$$L = \sqrt{h^2 + r^2} \tag{7}$$

where r is the distance on the wall surface from the center where the gas bubble exists directly above it, $R_{g,min}$ is the gas bubble radius at which $p_{L,max}$ occurs when the bubble contracts, and L is the distance from the bubble center to any position on the solid wall surface as expressed in Equation (7). The MICP applied on the solid wall varies with not only $p_{L,max}$ but also the distance from the bubble center to the wall surface, h.

Figure 11 shows the relationship between the initial gas bubble radius and the normalized MICP applied on the solid wall, $P^*_{imp,r=0}$, for different distances of the gas bubble to the solid wall, h, for $p_{\infty,1} = -0.02$ MPa and $t_1 = 5$ ms. MCIP applied on the solid wall, $P^*_{imp,r=0}$, depended on not only the radius of the initial gas bubble but also with the distance between the gas bubble and h. $P^*_{imp,r=0}$ became larger when larger gas bubbles existed near the wall.
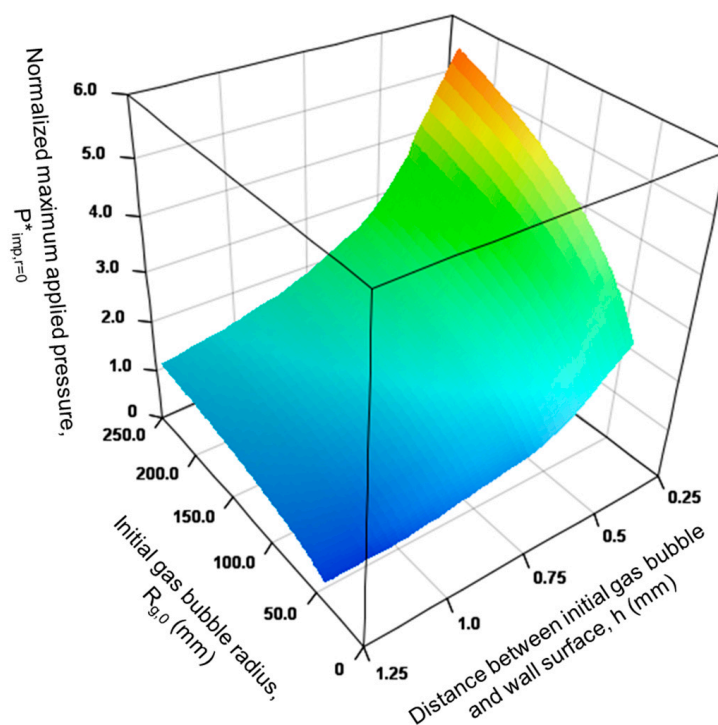
Figure 11. Relationship between the initial gas bubble radius and the maximum applied pressure on the wall surface, $P_{imp,r=0}$, for different distances between the gas bubble and the solid wall, h, in the case of $p_{\infty,1} = -0.02$ MPa and $t_1 = 5$ ms. The maximum applied pressure, $P_{imp,r=0}$, increased with increases in $R_{g,0}$ and decreases in h.

4. Discussion

4.1. The Generation Mechanism of Streak-like Defects with Beaded Pits

As shown in Figure 3, the damage was mitigated by the stable injection of gas bubbles to reduce MACPs. On the other hand, damage that might have been caused by the gas bubbles was observed. In this section, the generation mechanism of the streak-like defects with beaded pits is discussed. The following are possible reasons for the generation of damage caused by the gas bubbles.

(A) Generation of isolated pits

Figure 12 shows a photograph of a series of the isolated pits together with the pressure history emitted from the gas bubble (Enlarged Figure 9). As shown in Figure 12, the gas bubble near the solid wall vibrated by being subjected to the macroscopic pressure changes and the MICP emitted when the gas bubble contracted. The local impact pressure caused the plastic deformation to form a pit on the solid wall. In the photograph of Figure 12, the isolated pits were aligned with a slope consistent with the trajectory of the gas bubbles shown in Figure 4. The radius of the pits decreased with the direction of the gas bubble travel, and the distance between the pits became smaller. On the other hand, in the numerical results, local impact pressure was generated when the bubble contracted, and the local impact pressure decreased with the number of contractions. As such, the time interval between the next pressure generation incident became short. These results reproduce the observed results. That is, a series of isolated pits can be caused by the vibration of a single gas bubble.
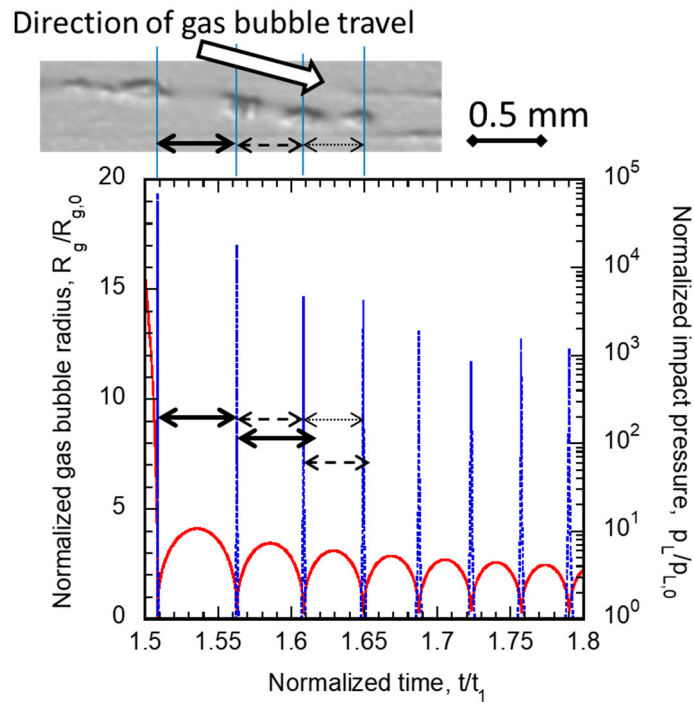
Figure 12. Photograph of a series of the isolated pits together with the pressure history emitted from the gas bubble (Enlarged Figure 9).

(B)   Generation of the streak-like defects

In a mercury target, about 10^8 pulsed proton beams were injected during the lifetime of the vessel. It is thought that the continuous pits overlap in the paths where the gas bubbles pass more frequently, as shown in Figure 13, resulting in streak-like defects.
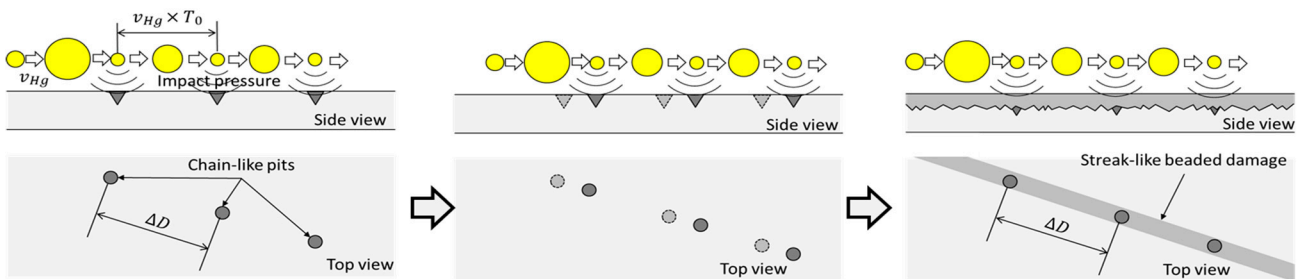
Figure 13. Formation mechanism of the streak-like defect with beaded pits.

(C)   Formation of bead-like continuous pits over the streak-like defects

It is thought that gas bubbles pass over the streak defects, and the miniscule impact pressure released by the vibration of the gas bubbles forms a series of beaded pits in the streak-like defects.

4.2. The Effect of the Initial Bubble Radius on the Generation of Isolated Pits

As shown in Figure 11, the MICP applied on the solid wall, $P_{imp}(r)$, depended on the gas bubble diameter, $R_{g,0}$, and the distance between the gas bubble and the wall, h. In the mercury target, larger gas bubbles were distributed in the upper part of the target (Area 1) than in the lower part (Area 2) as shown in Figure 2, and thus larger pits were expected to be observed in the Area 1. However, the observations shown in Figure 7 showed no significant difference in pit depth between Area 1 (upper) and Area 2 (lower), although the pit radius was larger in Area 1. The applied pressure on the wall depends not on the

initial bubble radius, $R_{g,0}$, but also on the distance between the bubble and wall, h, as shown in Figure 11. Therefore, we discuss the distance between the gas bubble and the wall surface. Figure 14 showed a distribution in the radial direction of the MICP applied on the solid wall, $P_{imp}(r)$, while varying $R_{g,0}$ and h. Comparing $P_{imp}(r)$ with the same $R_{g,0}$, $P_{imp}(r = 0\ \mu m)$ became larger with decreased of h. However, $P_{imp}(r > 150\ \mu m)$ was almost similar. On the other hand, comparing $P_{imp}(r)$ with same h, $P_{imp}(r = 0\ \mu m)$ was larger when R_g was larger, regardless of r. These results indicated that larger bubbles existing away from the solid wall and small bubbles existing near the solid wall generate pits with similar depth, but the former generates relatively wide pits.
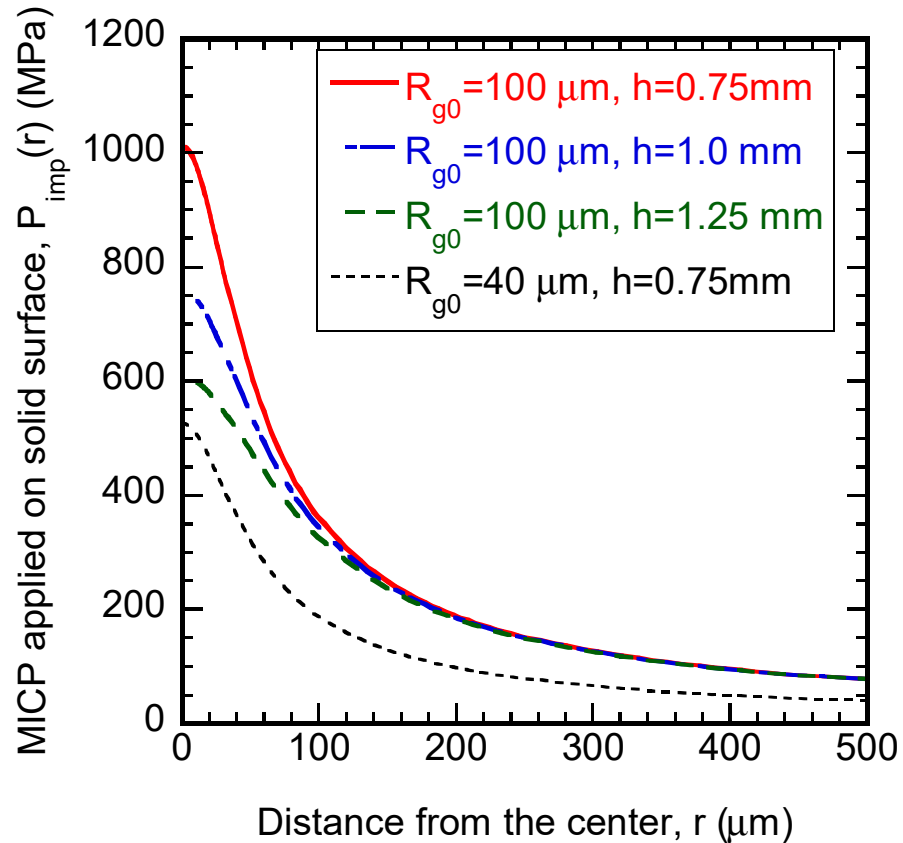
Figure 14. Distribution in the radial direction of the MICP applied on the solid wall, $P_{imp}(r)$, while varying $R_{g,0}$ and h.

Gas bubbles flowing near the wall are subject to centripetal force and drag force due to wall interaction. Near the beam window, bubbles tend to move away from the beam window due to the centripetal force caused by the upstream corners in the mercury target. The mercury flow bends from the entrance side to the beam window. Therefore, centripetal force acts on the bubbles toward the center of the radius of curvature. The centripetal force acting on the bubbles in the flow is generally expressed as shown in Equation (8), which depends on the size of the bubble diameter, like the buoyancy force.

$$F_c = \rho \times a \times \frac{4}{3}\pi R_{g,0}^3 \tag{8}$$

where a is the acceleration of the mercury in the direction of the center of curvature in the corner.

Guan et al. calculated the trajectory of a gas bubble rising near a wall in a static liquid and showed that the gas bubble rises while leaving the wall. And, when the bubble's Reynolds number is high, i.e., the bubble radius is large, the distance between the bubble

leaving the wall while rising becomes larger due to the lift generated by the influence of the wall surface [21]. In the mercury target vessel, the large bubbles were considered to be moving away from the wall, resulting in the applied local pressure, $P_{imp}(r)$, equivalent to that of the small bubbles.

5. Concluding Remarks

In the mercury target vessel of a spallation neutron source, it has been recognized that gas microbubbles reduce the MACPs caused by the thermal expansion of mercury due to proton beam injection. On the other hand, the mechanism of damage formation by the MICP emitted by the gas bubbles' vibration was considered in the formation of isolated pits, streak-like defects, and the beaded pits in these defects, which had not been observed under low proton beam power. The knowledge obtained in this study is as follows:

(1) As a result of operating the mercury target at a high proton beam power with sufficient injection of gas microbubbles, streak-like defects with beaded pits were observed in the mercury target vessel. The direction of the streak-like defects were almost consistent with the flow direction of the gas bubbles estimated by CFD analysis. The distance between the continuous beaded pits observed on the streak-like defects was wider in the upper area than in the lower area in the gravity direction. The distance to the next pit on the beaded pits was estimated assuming that the gas bubbles moved with mercury flow velocity and pits were formed by the natural period of bubble vibration, based on the bubble distribution results from the CFD analysis. The distance was wider in the upper area where more large bubbles were distributed, which was consistent with the observation results;

(2) In the estimation based on the Keller-Miksis equation, the gas bubbles expanded, then contracted, and repeated the expansion and contraction again. The MICP was emitted in each contraction. The MICP emitted by the gas bubble vibrations decreased with the number of repetitions of the vibration and its period became shorter. In the observed series of isolated pits, the damage size decreased and the distance between the pits became shorter in the flow direction of the gas bubble. These results indicated a correlation between the motion of the gas bubbles and the damage;

(3) The MICP applied on the solid wall, which were generated in the contractions of gas bubbles, could be sufficient to generate the plastic deformation and pits in the wall material. The applied pressure on the solid wall was higher when the initial radius of the gas bubble was larger and when the gas bubble existed closer to the solid wall;

(4) In the observed damage, in the upper area of the gravity direction where many of the gas bubbles with a large initial radius existed, the pit radius tended to be large, although the maximum pit depth was similar to those in the lower area. This was considered that the large gas bubbles were further away from the wall surface than the small gas bubbles and the maximum MICP applied on the solid wall surface was similar in the upper and lower areas.

In this paper, we showed the potential of gas microbubbles in causing damage on solid wall surfaces. In the mercury target, gas microbubbles reduce MACPs, resulting in suppressing cavitation damage. On the other hand, the gas microbubbles emit MICP, which causes the damage. Increasing the number of gas microbubbles is effective, but the gas bubbles may become cavitation nuclei which emit MICP. It will be important to optimize the number of gas bubbles to be injected, taking into account the interaction of multiple gas bubbles for the operation with a higher proton beam power and longer lifetime of the mercury target vessel. In addition, for various application techniques using gas microbubbles, especially when damage is a concern, it is necessary to consider the local

impact pressure emitted from the gas bubbles themselves as shown in this paper, not only the microjets generated in the bubbles collapsing near the solid wall.

References

1. Hashim, A.; Yaakob, O.B.; Koh, K.K.; Ismail, N.; Ahmed, Y.M. Review of Micro-bubble Ship Resistance Reduction Methods and the Mechanisms that Affect the Skin Friction on Drag Reduction from 1999 to 2015. *J. Teknol.* **2015**, *74*, 105–114. [CrossRef]
2. Takahashi, M. Microbubble: Fundamental Properties and Application for Semiconductor Cleaning. *J. Jpn. Soc. Precis. Eng.* **2017**, *83*, 636–640. [CrossRef]
3. Chomas, J.E.; Dayton, P.; Allen, J.; Morgan, K.; Ferrara, K.W. Mechanisms of contrast agent destruction. *Trans. Ultrason. Ferroelectr. Freq. Control* **2001**, *48*, 232–248. [CrossRef] [PubMed]
4. Available online: https://neutrons.ornl.gov/ (accessed on 20 September 2024).
5. Available online: https://j-parc.jp/c/en/index.html (accessed on 20 September 2024).
6. Robert TKnapp, R.T. Recent Investigations of the Mechanics of Cavitation and Cavitation Damage. *Trans. Am. Soc. Mech. Eng.* **1955**, *77*, 1045–1054.
7. Plesset, M.S.; Chapman, R.B. Collapse of an Initially Spherical Vapour Cavity in the Neighbourhood of a Solid Boundary. *J. Fluid Mech.* **1971**, *47*, 283–290. [CrossRef]
8. Futakawa, M.; Kogawa, H.; Hino, R.; Date, H.; Takeishi, H. Erosion damage on solid boundaries in contact with liquid metals by impulsive pressure injection. *Int. J. Impact Eng.* **2003**, *28*, 123–135. [CrossRef]
9. Kogawa, H.; Futakawa, M.; Ishikura, S. Dynamic Response of Mercury Subjected to Pressure Wave. *J. Nucl. Sci. Technol.* **2007**, *44*, 523–529. [CrossRef]
10. Futakawa, M.; Kogawa, H.; Hasegawa, S.; Naoe, T.; Ida, M.; Haga, K.; Wakui, T.; Tanaka, N.; Matsumoto, Y.; Ikeda, Y. Mitigation technologies for damage induced by pressure waves in high-power mercury spallation neutron sources (II)—Bubbling E. ect to Reduce Pressure Wave—. *J. Nucl. Sci. Technol.* **2008**, *45*, 1041–1048. [CrossRef]
11. Kogawa, H.; Naoe, T.; Kyotoh, H.; Haga, K.; Kinoshita, H.; Futakawa, M. Development of microbubble generator for suppression of pressure waves in mercury target of spallation source. *J. Nucl. Sci. Technol.* **2015**, *52*, 1461–1469. [CrossRef]
12. Kogawa, H.; Naoe, T.; Futakawa, M.; Haga, K.; Wakui, T.; Harada, M.; Takada, H. Mitigation technologies for damage induced by pressure waves in high-power mercury spallation neutron sources (IV)—Measurement of pressure wave response and microbubble effect on mitigation in mercury target at J-PARC—. *J. Nucl. Sci. Technol.* **2017**, *54*, 733–741. [CrossRef]
13. Ida, M.; Naoe, T.; Futakawa, M. Suppression of cavitation inception by gas bubble injection: A numerical study focusing on bubble-bubble interaction. *Phys. Rev. E* **2007**, *76*, 046309. [CrossRef] [PubMed]
14. Ida, M.; Naoe, T.; Futakawa, M. On the effect of microbubble injection on cavitation bubble dynamics in liquid mercury. *Nucl. Instrum. Methods Phys. Res. Sect. A Accel. Spectrometers Detect. Assoc. Equip.* **2009**, *600*, 367–375. [CrossRef]
15. Naoe, T.; Kinoshita, H.; Wakui, T.; Kogawa, H.; Haga, K. *Technical Note for the Cavitation Damage Inspection for Interior Surface of the Mercury Target Vessel (1) Development of Specimen Cutting Machine for Remote Handling. JAEA-Technology 2022-018*; Japan Atomic Energy Agency: Ibaraki, Japan, 2022. (In Japanese)
16. Kogawa, H.; Haga, K.; Futakawa, M.; Tsuzuki, T.; Murai, T. *Optimization of Mercury Flow with Microbubbles in the Target-Vessel Design by Means of Machine Learning. JAEA-Technology 2022-023*; Japan Atomic Energy Agency: Ibaraki, Japan, 2022. (In Japanese)

17. Kameda, M.; Yamada, M.; Matsumoto, Y. Motion of a Spherical Bubble in an Oscillatory Pressure Field. *Trans. JSME (B)* **1998**, *64*, 1650–1658. (In Japanese) [CrossRef]

18. Futakawa, M.; Naoe, T.; Kogawa, H.; Date, H.; Ikeda, Y. Micro-Impact Damage Caused by Mercury Bubble Collapse. *JSME Int. J. Ser. A* **2005**, *48*, 234–239. [CrossRef]

19. Keller, J.B.; Miksis, M. Bubble oscillations of large amplitude. *J. Acoust. Soc. Am.* **1980**, *68*, 628–633. [CrossRef]

20. Kandula, M.; Freeman, R. On the Interaction and Coalescence of Spherical Blast Waves. *Shock Waves* **2008**, *18*, 21–33. [CrossRef]

21. Guan, C.; Yanase, S.; Matsuura, K.; Kouchi, T.; Nagata, Y. Numerical Study on Motion of a Single Spherical Bubble near Vertical Wall in the quiescent Fluid using the Modified Force-Coupling Method. *Nagare* **2018**, *37*, 281–289. (In Japanese)